# Persistent Non-Gaussian Correlations in Out-of-Equilibrium Rydberg Atom Arrays

Aydin Deger[,1,2,*] Aiden Daniel[,2] Zlatko Papić[,2] and Jiannis K. Pachos[2]

[1]*Department of Physics and Astronomy, University College London, London, WC1E 6BT, United Kingdom*

[2]*School of Physics and Astronomy, University of Leeds, Leeds, LS2 9JT, United Kingdom*

Gaussian correlations emerge in a large class of many-body quantum systems quenched out of equilibrium, as demonstrated in recent experiments on coupled one-dimensional superfluids [Schweigler *et al.*, Nat. Phys. 17, 559 (2021)]. Here we present a mechanism by which an initial state of a Rydberg atom array can retain persistent *non-Gaussian* correlations following a global quench. This mechanism is based on an effective kinetic blockade rooted in the ground state symmetry of the system, which prevents thermalizing dynamics under the quench Hamiltonian. We propose how to observe this effect with Rydberg atom experiments and we demonstrate its resilience regarding several types of experimental error. These long-lived non-Gaussian states may have practical applications as quantum memories or stable resources for quantum information protocols due to the protected non-Gaussianity away from equilibrium.

## I. INTRODUCTION

Free-field theories describe the dynamics of fields with no interactions. These are known as Gaussian as their path integral description contains some form of Gaussian function [1,2]. In the presence of interactions, however, the system's ground state often develops strong non-Gaussian correlations. While Gaussian states are highly structured and can be understood with use of a variety of theoretical techniques, it is the non-Gaussian states that often play a key role as resources for universal quantum computation and increasing the efficiency of a range of quantum information protocols, including quantum teleporation, communication, sensing, metrology, and quantum error correction [3–15].

Recent studies have investigated the behavior of quantum states under nonequilibrium dynamics, sparked by the intriguing question of what happens to an interacting state when interactions suddenly vanish, for example, after a global quench of the system. It has been shown that generic closed systems, governed by quadratic Hamiltonians, swiftly relax to Gaussian states, regardless of their initial condition, in contrast to recent results established in finely tuned open quantum system [16,17]. This can

be viewed as an example of a "quantum central limit" theorem [18,19]. To explain the emergence of Gaussianity, several mechanisms have been proposed, such as spatial scrambling and canonical transmutation, the latter suggesting that Gaussian components of the initial system act as a Gaussian bath, suppressing non-Gaussianity [16,20]. These mechanisms have been used to describe the decay of non-Gaussianity in recent experiments on $^{87}$Rb superfluids trapped in a double-well potential [21,22]. While these studies have provided crucial insights into the process of relaxation in quantum many-body systems [23], they are restricted to systems with effectively noninteracting degrees of freedom, which do not exhibit "full" thermalization but relax only towards a generalized Gibbs ensemble [24]. It is thus important to understand the role of Gaussianity in interacting systems, which can exhibit chaotic dynamics and thermalization. In particular, it is important to understand if and how non-Gaussianity could be protected in such many-body systems when they are taken out of their equilibrium state.

In this paper, we show that Rydberg atom arrays [25] provide a versatile experimental platform for realizing and manipulating non-Gaussian correlations far from equilibrium. We show that quenching the atoms between different ordered phases allows one to explore two very different regimes of correlations. On the one hand, our setup allows one to observe how non-Gaussian correlations build up as the system undergoes thermalizing dynamics from an initial, nearly free-fermion state. On the other hand, it is possible to "lock" the system in a strongly non-Gaussian state, which evades both Gaussification and thermalization
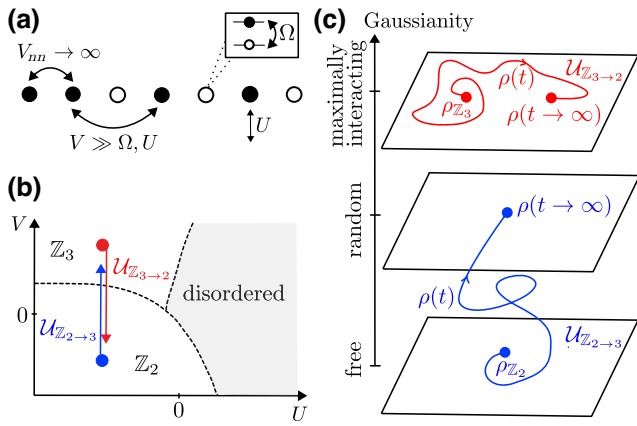
*aydindeger@icloud.com

FIG. 1. (a) One-dimensional Rydberg atom model. (b) Phase diagram in the $U$-$V$ plane. We focus on the $\mathbb{Z}_2$ and $\mathbb{Z}_3$ ordered phases and quenches between them: the blue arrow indicates a quench from the $\mathbb{Z}_2$ ordered phase into the $\mathbb{Z}_3$ phase, $\mathcal{U}_{\mathbb{Z}_{2\rightarrow 3}}$, while the red arrow represents the reverse quench, $\mathcal{U}_{\mathbb{Z}_{3\rightarrow 2}}$. (c) The two types of quench lead to strikingly different dynamical behaviors. During the $\mathcal{U}_{\mathbb{Z}_{2\rightarrow 3}}$ quench, the system is initially free and Gaussianity grows until it reaches typical values in a random state. By contrast, during the $\mathcal{U}_{\mathbb{Z}_{3\rightarrow 2}}$ quench, the state remains strongly interacting and it is pinned to a highly non-Gaussian manifold. We quantify this picture in Secs. III and IV using precise Gaussianity measures.

at late times. This intriguing non-Gaussian regime is found to be remarkably robust, for example, even with regard to quenching the system across a quantum phase transition. Our proposal can be readily implemented in Rydberg atom experiments [26–29], which have recently realized the required types of ordered states and protocols for probing correlations in out-of-equilibrium dynamics.

The remainder of this paper is organized as follows. In Sec. II we introduce our model of Rydberg atom arrays and summarize our main results, which are illustrated in Fig. 1. In Sec. III we introduce our approach for quantifying Gaussianity, using two complementary diagnostics: the Wick decomposition in terms of local correlations that are experimentally accessible, and a more general measure based on reduced density matrix and variational optimization [30]. We apply these tools to obtain the Gaussianity phase diagram of a one-dimensional Rydberg atom array. In Sec. IV we study dynamics of Gaussianity under global quenches connecting different regions of the phase diagram, whose underlying mechanism is elucidated in Sec. V. In Sec. VI we demonstrate the resilience of our results in the face of potential experimental errors, such as local impurity potentials and longer-range interactions. Our conclusions are presented in Sec. VII, while the appendixes contain technical details on the choice of operators in the Wick decomposition, finite-size scaling analysis, and the role of the boundary conditions.

## II. THE MODEL

We consider a one-dimensional periodic chain containing $N$ Rydberg atoms. Each atom is modeled as a two-level system, where $|0\rangle$ represents an atom in the ground state and $|1\rangle$ is an excited (Rydberg) state. The atomic array is governed by the Hamiltonian [31]

$$\mathcal{H} = \sum_{i=1}^{N} -\Omega \mathcal{P}_{i-1} \sigma_i^x \mathcal{P}_{i+1} + U n_i + V n_i n_{i+2}, \quad (1)$$

where $\sigma^x = |0\rangle\langle 1| + |1\rangle\langle 0|$ is the Pauli $x$ operator, $n = |1\rangle\langle 1|$ is the local density operator, and $\mathcal{P} = |0\rangle\langle 0|$ is the projector on the ground state at a given site. The flipping between the ground state and the excited state is described by the Rabi frequency $\Omega$, $U$ is the chemical potential (detuning), and $V$ is the next-nearest-neighbor interaction between atoms excited to Rydberg states; see Fig. 1(a). Unless specified otherwise, because of the periodic boundary conditions (PBCs), we restrict our calculations to the zero-momentum sector.

The model in Eq. (1) is applicable to the strong Rydberg blockade regime, where the magnitude of the nearest-neighbor van der Waals interaction is much larger than all other couplings of the model [25]. The strong Rydberg blockade imposes the kinetic constraint $n_i n_{i+1} = 0$, which forbids Rydberg excitations on adjacent sites. This constraint is enforced in the Hamiltonian by the dressing of the $\sigma_i^x$ with projectors $\mathcal{P} = |0\rangle\langle 0|$ on the neighboring atoms. This prevents the Rabi flip term from generating nearest-neighbor excitations, such that states $\cdots 11 \cdots$ with neighboring atoms simultaneously excited are projected out of the Hilbert space. The constraint results in the effective model in Eq. (1), which is also known as the PXP model [32,33].

The interplay of $U$ and $V$ gives rise to a rich phase diagram, as sketched in Fig. 1(b). The phase diagram was mapped out with high precision in the numerical simulations in Refs. [34–36] and was explored in experiments [27,28]. Large negative values of the chemical potential $U$ favor excitations on every other site (due to the Rydberg blockade, this is largest density of excitations allowed). On the other hand, positive $V$ assigns a repulsive potential on the next-nearest neighbors and it favors excitations on every third site. Conversely, large negative $V$ favors excitations on every other site. Thus, the model in Eq. (1) hosts two ordered phases represented by the states

$$|\mathbb{Z}_2\rangle = \frac{1}{\sqrt{2}}(|10101\ldots\rangle + |01010\ldots\rangle), \quad (2)$$

$$|\mathbb{Z}_3\rangle = \frac{1}{\sqrt{3}}(|100100\ldots\rangle + |010010\ldots\rangle + |001001\ldots\rangle),$$

$$(3)$$

in which Rydberg excitations occupy every second or third site, respectively. Both these phases are destroyed by sufficiently large positive $U$, which drives the system into a disordered phase; see Fig. 1(b) [31,37,38].

For the subsequent calculations, unless specified otherwise, we set $\Omega = 1$ and concentrate on the Gaussianity and entanglement properties of the initial state as we quench the Hamiltonian between $\mathbb{Z}_2$ and $\mathbb{Z}_3$ ordered phases; see Fig. 1(b). We show that the choice of the initial state and realization of the quench can have dramatically different influences on the Gaussianity, as illustrated in Fig. 1(c). For the quench initialized in the $\mathbb{Z}_2$ phase, indicated by $\mathcal{U}_{\mathbb{Z}_{2\to3}}$ in Fig. 1(b), the Gaussianity, as precisely defined in Sec. III, is initially low because the prequench state can be approximately expressed as a free-fermion state. After the quench, the state becomes progressively more correlated, with its Gaussianity approaching that of a random vector in the same Hilbert space at late times. This behavior is consistent with thermalization dynamics. In contrast, the ground state in the $\mathbb{Z}_3$ phase cannot be expressed as a free-fermion state and hence it has high non-Gaussianity. Moreover, following the quench, the state remains strongly interacting, which occurs due to a lack of thermalization in this case. It is important to note that in both cases the quench Hamiltonian, regardless of the nature of the ground state, is an interacting, nonintegrable Hamiltonian—further contrasting the two regimes. In the following sections, we introduce several metrics of non-Gaussianity and quantitatively support the phase diagram and dynamical behavior sketched in Fig. 1.

## III. GAUSSIANITY PHASE DIAGRAM

A conventional approach for quantifying the Gaussianity of quantum states relies on Wick's theorem [1]. This theorem allows one to reduce the evaluation of $n$-point correlation functions in terms of "contractions" (i.e., vacuum expectation values) of pairs of creation and annihilation operators. For any free-fermion system, Wick's identity for four-point correlators takes the form

$$\langle \hat{A}\hat{B}\hat{C}\hat{D} \rangle = \langle \hat{A}\hat{B} \rangle \langle \hat{C}\hat{D} \rangle - \langle \hat{A}\hat{C} \rangle \langle \hat{B}\hat{D} \rangle + \langle \hat{A}\hat{D} \rangle \langle \hat{B}\hat{C} \rangle, \quad (4)$$

where the expectation value is with respect to the ground state ("vacuum"). One possible definition of Gaussianity $\mathcal{W}$ is the extent to which Eq. (4) is violated, i.e., the absolute value of the difference between its left-hand side and its right-hand side. For Gaussian states, we have $\mathcal{W} = 0$. The operators $\hat{A}, ..., \hat{D}$ are understood to be single-site fermionic creation and annihilation operators $\hat{f}_i, \hat{f}_j^\dagger$, which obey the anticommutation relation $\{\hat{f}_i, \hat{f}_j^\dagger\} = \delta_{ij}$. As our model in Eq. (1) is expressed in terms of spin variables, it will be convenient to work with spin operators rather than fermionic ones, which can be accomplished by applying the Jordan-Wigner transformation.

To distinguish the Gaussianity between $\mathbb{Z}_2$ and $\mathbb{Z}_3$ ordered phases, we choose $\hat{A} = \hat{f}_1^\dagger$, $\hat{B} = \hat{f}_1$, $\hat{C} = \hat{f}_2^\dagger$, and $\hat{D} = \hat{f}_3$, resulting in the following measure of the Wick decomposition violation:

$$\mathcal{W}(\rho) = \big| \langle n_1 \sigma_2^+ \sigma_3^- \rangle - \langle n_1 \rangle \langle \sigma_2^+ \sigma_3^- \rangle$$
$$- \langle \sigma_1^+ \sigma_2^+ \rangle \langle \sigma_1^- \sigma_2^z \sigma_3^- \rangle + \langle \sigma_1^- \sigma_2^+ \rangle \langle \sigma_1^+ \sigma_2^z \sigma_3^- \rangle \big|,$$
$$(5)$$

where $\sigma_j^\pm \equiv (\sigma_j^x \mp i\sigma_j^y)/2$ are the standard spin-raising and spin-lowering operators at site $j$ and where $\rho$ denotes the ground state of the system (which could be either a pure state or a density matrix). This particular choice of operators $\hat{A}, ..., \hat{D}$ is justified in Appendix A; it reveals the difference between the $\mathbb{Z}_2$ phase, where $\mathcal{W} \approx 0$ across the entire phase, and the $\mathbb{Z}_3$ phase, where the deviation from the Wick decomposition is of order unity, $\mathcal{W} \sim O(1)$.

The ambiguity in the choice of operators in the Wick decomposition can be eliminated by use of variational optimization techniques to measure the minimum distance between the reduced density matrix of a given state and the set of all density matrices associated with free-fermion models [30,39–41]. This quantity, dubbed the "interaction distance" $D_{\mathcal{F}}$ [30], allows a more general characterization of the state's Gaussianity by quantifying its deviation from the *closest* free-fermion model defined in an *arbitrary* basis. Interaction distance is a property of the reduced density matrix $\rho$ describing the subsystem $A$ of a bipartite system $A \cup B$. For the total system in a pure state $|\psi\rangle$, the reduced density matrix $\rho = \mathrm{tr}_B |\psi\rangle \langle\psi|$ is obtained by tracing out the subsystem $B$, and its eigenvalues $\rho_k$ define the so-called entanglement spectrum, $\mathcal{E}_k = -\ln \rho_k$ [42]. With use of the entanglement spectrum, the interaction distance is defined as

$$D_{\mathcal{F}}(\rho) = \min_{\{\epsilon\}} \frac{1}{2} \sum_k \left| e^{-\mathcal{E}_k} - e^{-\mathcal{E}_k^f(\epsilon)} \right|, \quad (6)$$

where $\mathcal{E}_k^f(\epsilon) = \sum_l n_l^{(k)} \epsilon_l$ is the entanglement spectrum of a free-fermion system, given in terms of single-fermion modes $\epsilon_l$ and their occupations $n_l^{(k)} \in \{0, 1\}$ [43]. The sum runs over the many-body entanglement spectrum. The minimization is over the single-particle energies $\{\epsilon\}$, whose number typically scales linearly with the number of atoms $N$.

It is worth noting that the entanglement spectrum is naturally dependent on the choice of bipartition. In this work, we consider a bipartition of the system into equal parts. Our results, however, are not sensitive to the particular choice of partition, as long as both subsystems are of comparable size. If one subsystem is much smaller than the other, the number of Schmidt coefficients will be significantly reduced and we expect nonuniversal behavior of $D_{\mathcal{F}}$. Interestingly, the interaction distance can also

be probed with respect to the eigenspectrum of the system—thus probing the thermal properties of a given Hamiltonian. This analysis can be done and reveals that in both ordered regimes the Hamiltonian is interacting. Generally, however, this is more cumbersome to perform with increasing system size due to the exponential scaling and does not reveal the distinct differences in the ground state between the two regimes.

Intuitively, $D_{\mathcal{F}}$ represents the minimum distance between the reduced density matrix of a given quantum state $\rho$ and the density matrix of the closest free-fermion model defined on the subsystem $A$. Crucially, the free-fermion model is defined up to an arbitrary unitary transformation on $A$, which makes $D_{\mathcal{F}}$ basis independent. This allows one to quantify the Gaussianity of a quantum state without the need to search for suitable operators in $\mathcal{W}$ as done in Eq. (5). However, $\mathcal{W}$ has the advantage over $D_{\mathcal{F}}$ in that it is expressed in terms of local correlations that are amenable to experimental measurements. Thus, Eq. (5) provides a more practical way of detecting non-Gaussianity in the laboratory.

The Gaussianity phase diagram for the ground state of the Hamiltonian in Eq. (1) is presented in Fig. 2 for a range of $U$ and $V$ values. The phase diagram was obtained with use of both the interaction distance $D_{\mathcal{F}}$ and the Wick's theorem violation $\mathcal{W}$, shown in Fig. 2(a) and 2(b). In Fig. 2(c) we show the von Neumann entanglement entropy, $S(\rho) = -\sum_k \rho_k \ln \rho_k$. All the quantities were computed for the reduced density matrix corresponding to the subsystem $A$ being half of the chain. Figure 2 reveals excellent qualitative agreement between all three metrics, in particular, between interaction distance and Wick decomposition. The phase boundaries are in good agreement with the phase boundaries in Refs. [34,36], suggesting weak finite-size effects. For large and negative chemical potential $U$, there are two competing ordered phases, $\mathbb{Z}_2$ and $\mathbb{Z}_3$. In particular, for large and positive values of $V$, the

ground state is the $\mathbb{Z}_3$ ordered state. The quantum phase transition from the $\mathbb{Z}_3$ ordered state to the $\mathbb{Z}_2$ ordered state occurs at $|V| \sim -U/3$. In between these two ordered phases, we expect a narrow intermediate commensurate phase [28,31,34], which is difficult to resolve in the small systems used in Fig. 2, but this phase is unimportant for our discussion.

Figures 2(a) and 2(b) reveal a stark contrast between the two ordered phases in terms of the Gaussian nature of their ground-state correlations: while the $\mathbb{Z}_2$ ground state is approximately a noninteracting Gaussian state with both $D_{\mathcal{F}}$ and $\mathcal{W}$ close to zero, the $\mathbb{Z}_3$ ground state is a nearly maximally interacting, non-Gaussian state. The notion of "maximally interacting" can be made precise by noting that $D_{\mathcal{F}}$, as a trace distance between density matrices, has an upper bound, which has been conjectured to be $D_{\mathcal{F}}^{\max} = 3 - 2\sqrt{2}$ [44]. In the $\mathbb{Z}_3$ phase in Fig. 2, $D_{\mathcal{F}}$ attains values very close to this upper bound, strongly suggesting that it is not possible to express the $\mathbb{Z}_3$ ground state as a Gaussian state of free-fermionic modes. Finally, we note that the entanglement entropy in Fig. 2(c) also captures some features of the phase diagram, but it does not sharply distinguish between the $\mathbb{Z}_2$ phase and the $\mathbb{Z}_3$ phase. Thus, the interaction distance and local Wick decomposition are essential to gain a complete understanding of non-Gaussianity, both in equilibrium as well as out of equilibrium, as we show next.

## IV. PERSISTENT NON-GAUSSIAN CORRELATIONS UNDER QUENCH

We have seen that the two competing ordered phases, $\mathbb{Z}_2$ and $\mathbb{Z}_3$, are the extreme points on the Gaussianity spectrum: while the $\mathbb{Z}_2$ ground state represents a nearly-free fermion state, the $\mathbb{Z}_3$ state is maximally interacting. It is natural to inquire about the temporal evolution of Gaussianity following a sudden quench between these phases. According to the standard scenario of thermalization in a closed system [45], under quench dynamics, particularly across a quantum phase transition, the system should lose memory of its initial state and equilibrate towards a maximally entangled state. To test this expectation, we study the spreading of entanglement and non-Gaussian correlations when the system is prepared in the ground state of the Hamiltonian (1) for some value $V \equiv V_i$. We then quench the Hamiltonian to some different value of $V \equiv V_f \neq V_i$. By varying $V_i$ and $V_f$, we can access different ordered states and postquench Hamiltonians. For simplicity, we keep $U$ the same in the initial Hamiltonian and the postquench Hamiltonian and postpone the discussion of its role to Sec. VI.

Figure 3(a) contrasts the growth of entanglement entropy for the $\mathcal{U}_{\mathbb{Z}_2 \to 3}$ quench versus the $\mathcal{U}_{\mathbb{Z}_3 \to 2}$ quench. In the first case, the system exhibits thermalization, as
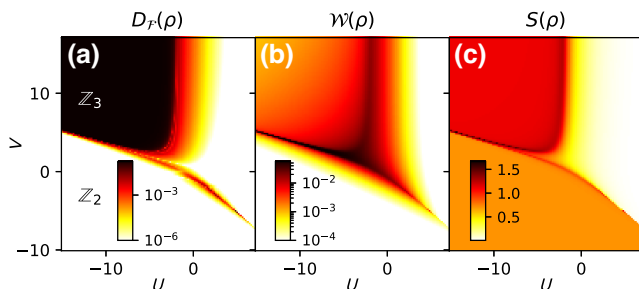


FIG. 2. Gaussianity phase diagram for the ground state of the model in Eq. (1) as a function of $U$ and $V$. The color scale represents the interaction distance $D_{\mathcal{F}}$ in (a), the Wick decomposition violation $\mathcal{W}$ in (b), and the entanglement entropy $S$ in (c). All data were obtained by exact diagonalization for $N = 18$ atoms on a ring with periodic boundary conditions.
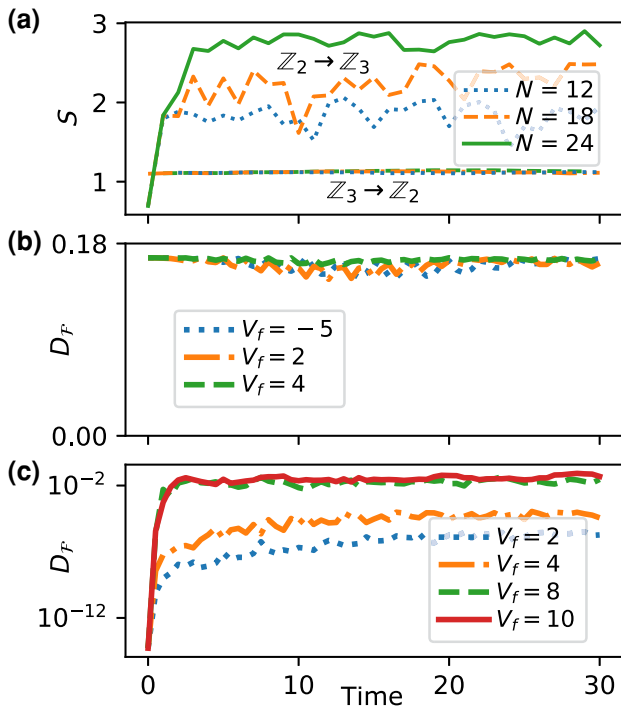
FIG. 3. Temporal behavior of entanglement and Gaussianity for quenches $\mathcal{U}_{\mathbb{Z}_2 \to 3}$ and $\mathcal{U}_{\mathbb{Z}_3 \to 2}$, as indicated in Fig. 1(b). The chemical potential $U$ is held fixed at $-15$. (a) Growth of entanglement entropy for different system sizes. The top three lines represent $\mathcal{U}_{\mathbb{Z}_2 \to 3}$ (specifically, $V_i = -5 \to V_f = 8$), while the bottom three (overlapping) lines are for the reverse quench, $\mathcal{U}_{\mathbb{Z}_3 \to 2}$. For the $\mathcal{U}_{\mathbb{Z}_2 \to 3}$ quench, the saturation entropy obeys the volume law scaling with system size, indicating thermalization. By contrast, the $\mathcal{U}_{\mathbb{Z}_3 \to 2}$ quench leads to strongly nonthermalizing dynamics, as evidenced by a complete lack of entropy growth. (b),(c) Temporal behavior of Gaussianity measured by interaction distance. In (b), the quench is from the $\mathbb{Z}_2$ ground state ($V_i = -5$) to a range of $V_f$ values spanning the $\mathbb{Z}_3$ and $\mathbb{Z}_2$ phases. The top plateau value corresponds to the interaction distance of a random state, $D_{\mathcal{F}}^{\text{random}} \approx 0.03$ [44], which is consistent with thermalization observed for $\mathcal{U}_{\mathbb{Z}_2 \to 3}$ in (a). (c) Similar to (b) but for the $\mathbb{Z}_3$ initial state ($V_i = 8$). The persistent large value of $D_{\mathcal{F}}$ is consistent with an absence of entanglement spreading for the $\mathcal{U}_{\mathbb{Z}_3 \to 2}$ quench in (a). The data in (b),(c) are for system size $N = 18$.

confirmed by the fast growth of entropy towards its saturation value when it reaches the thermal state. A key indication of thermalization is the volume-law scaling behavior of the saturation value of entanglement entropy, $S_\infty \propto N$, consistent with what is seen in Fig. 3(a). In contrast, quenches from the $\mathbb{Z}_3$ state lead to nonthermalizing dynamics, as seen in the strongly suppressed growth of entropy in Fig. 3(a).

In Fig. 3(b) we illustrate how Gaussianity changes in time when we prepare the system in an approximately Gaussian $\mathbb{Z}_2$ state at $t = 0$. In particular, when the postquench Hamiltonian is in the $\mathbb{Z}_3$ phase (e.g., $V_f = 8$), the deviation from Gaussianity sharply increases from

zero and quickly reaches the saturation value of $D_{\mathcal{F}}^\infty \approx 0.03$, which coincides with the interaction distance of a random vector [44]. This is consistent with the thermalizing dynamics at infinite temperature in Fig. 3(a), where the state at late times becomes similar to a random vector. Note that this scenario is very different from the scenario in Ref. [22], where the initial state was chosen to be non-Gaussian but the Hamiltonian itself is quadratic and induces the development of Gaussian correlations over time.

Conversely, for the non-Gaussian $\mathbb{Z}_3$ initial state in Fig. 3(c), we see that the previous scenario does not hold. In this case, there is persistent non-Gaussianity after the quench, with no sign of decay of the correlations due to interactions. Consequently, the time-evolved state remains highly interacting over the course of quantum dynamics. We note that these results hold for larger system sizes via finite-size scaling and with open boundary conditions (OBCs): see Appendix B.

We now analyze the $\mathcal{U}_{\mathbb{Z}_3 \to 2}$ quench in more depth. In terms of spectral properties, we find that there is a single energy eigenstate $|E_1\rangle$ of the Hamiltonian that has very high overlap with the $\mathbb{Z}_3$ state, $|\langle E_1 | \mathbb{Z}_3 \rangle|^2 \approx 1$; see Fig. 4(a). The energy of this eigenstate also exactly
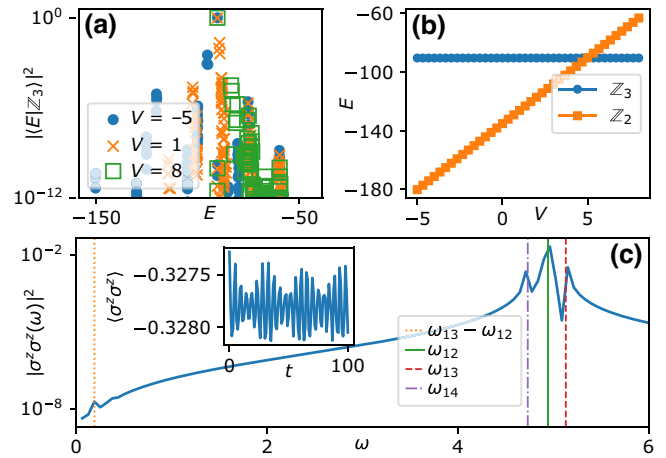


FIG. 4. Nature of the non-Gaussian quench $\mathcal{U}_{\mathbb{Z}_3 \to 2}$. (a) Overlap between the $\mathbb{Z}_3$ initial state [as defined in Eq. (2)] and energy eigenstates $|E\rangle$ of the Hamiltonian in Eq. (1) plotted as a function of energy. The data are for system size $N = 18$ and $U = -15$ for three $V$ values given in the legend. In all cases, the $\mathbb{Z}_3$ state has high support (overlap approximately 1) on a single eigenstate at roughly the same energy. (b) Energy expectation value, $E = \langle \psi | \mathcal{H} | \psi \rangle$, for product states $|\psi\rangle = |\mathbb{Z}_3\rangle$ and $|\psi\rangle = |\mathbb{Z}_2\rangle$ plotted as a function of $V$ with fixed $U = -15$. We see that $|\mathbb{Z}_3\rangle$ remains at constant energy for any $V$, while $|\mathbb{Z}_2\rangle$ scales linearly. (c) Power spectrum of the correlation function $\langle \sigma_i^z \sigma_{i+1}^z \rangle$ evaluated in the time-evolved state (raw data shown in the inset). The vertical lines in the plot represent the energy gaps $\omega_{ij}$ between the states with the largest overlap in (a). The gaps align precisely with the peaks in the power spectrum.

matches that of the ground state energy of the initial Hamiltonian prequench. The energy of the state is independent of deforming $V$ in the quench Hamiltonian as shown in Fig. 4(b). This implies that the $\mathbb{Z}_3$ state is effectively close to being an eigenstate of the Hamiltonian. This behavior is somewhat reminiscent of quantum many-body scarring [46–48], with the exception that here the high overlap exists only for a single eigenstate. Furthermore, numerically we find that the special eigenstate $|E_1\rangle$ has lower entanglement entropy than the majority of the spectrum, whereas its interaction distance attains a nearly maximum value. By also plotting the overlap between the $\mathbb{Z}_3$ state and the eigenstates of Hamiltonians with $V = 8$ and $V = 1$, we see the single eigenstate remains dominant at constant energy, regardless of the value of $V$, simply transitioning from being an initial ground state to a midspectrum state.

In Fig. 3(c), we see that non-Gaussianity remains robust for the quench $\mathcal{U}_{\mathbb{Z}_3 \to 2}$. To experimentally access this behavior, one can study temporal behavior of local correlation functions, as is frequently done in modern ultracold atom experiments [49]. For example, the correlation function $\langle \sigma_i^z \sigma_{i+1}^z \rangle$ [see Fig 4(c)] reveals persistent oscillations. The characteristic frequencies of these oscillations correspond to the energy differences of the eigenstates with dominant overlap with the initial state of the system. This can be characterized more precisely by the power spectrum [50,51]; see Fig. 4(c). The dominant frequencies are given by $\omega_{1j} = |E_1 - E_j|$ (and their differences), where $|E_j\rangle$, $j = 2, 3, \ldots$, denote eigenstates with subleading overlaps with the $\mathbb{Z}_3$ state. Similar oscillations and frequencies can be observed in the quantity $\mathcal{W}$ defined in Eq. (5), other two-point local correlations, and even in the entanglement entropy.

A simple heuristic argument that gives an approximate value of the oscillation frequency in the limit $U, V \gg \Omega$ can be stated as follows. For the Hamiltonian with $U = -15$ and $V = -5$, the ground state is approximately the $\mathbb{Z}_2$ product state with energy $E_{\text{GS}}^{\mathbb{Z}_2} \approx (U + V)N/2$. The energy of the $\mathbb{Z}_3$ state is $E^{\mathbb{Z}_3} \approx UN/3$. For general values of $U$ and $V$, there are no other states with the same energy as $\mathbb{Z}_3$. For special ratios of $U$ and $V$, a resonance may occur and other states could have the same energy as $\mathbb{Z}_3$; we can prevent this by assuming $U$ and $V$ to be irrational numbers. The oscillations seen in Fig. 4(c) are between $|\mathbb{Z}_3\rangle$ and states where one of the excitations is moved by a single unit, i.e., the states $|101000100100\ldots\rangle$, $|100101000100\ldots\rangle$ etc., which all have a single 101 pattern. The energy of these states is $UN/3 + V$, so they are lower in energy by approximately $-|V|$ compared with $\mathbb{Z}_3$. This predicts that the oscillation frequency is set by $V$, i.e., the energy difference between $\mathbb{Z}_3$ states and these states containing $|\ldots 101 \ldots\rangle$ in the chain. Thus, the energy differences between second and first energy levels are determined by $|V|$, i.e., $\omega_{12} = |E_1 - E_2| \approx |V|$, as can be seen in the power spectrum in Fig. 4(c).

## V. ORIGIN OF PERSISTENT NON-GAUSSIAN CORRELATIONS

The origin of robust non-Gaussianity associated with the $\mathbb{Z}_3$ state can be more readily understood by considering the evolution in eigenspace overlap for different $V$ presented in Fig. 4(a). We consider the difference between the initial Hamiltonian, $\mathcal{H}_i$, and the postquench Hamiltonian, $\mathcal{H}_f$. Recalling Fig. 1(b), we restrict ourselves to the case where the quench changes the value of only $V$. Therefore, $\mathcal{H}_f = \mathcal{H}_i + \Delta V \mathcal{H}^{nn}$, where $\mathcal{H}^{nn} = \sum_i n_i n_{i+2}$. Now consider a quench from the $\mathbb{Z}_3$ state in its respective regime such that $\mathcal{H}_i |\mathbb{Z}_3\rangle = E_0 |\mathbb{Z}_3\rangle$ with ground state energy $E_0$. Then quenching yields $\mathcal{H}_f |\mathbb{Z}_3\rangle = \mathcal{H}_i |\mathbb{Z}_3\rangle + \Delta V \mathcal{H}^{nn} |\mathbb{Z}_3\rangle$. Note that in the case of $|\mathbb{Z}_3\rangle$, there is occupancy of only every third site; therefore, $\mathcal{H}^{nn} |\mathbb{Z}_3\rangle = 0$, irrespective of $\Delta V$. Thus,

$$\mathcal{H}_f |\mathbb{Z}_3\rangle = \mathcal{H}_i |\mathbb{Z}_3\rangle + \Delta V \mathcal{H}^{nn} |\mathbb{Z}_3\rangle = \mathcal{H}_i |\mathbb{Z}_3\rangle = E_0 |\mathbb{Z}_3\rangle. \tag{7}$$

Hence, when $\Delta V$ is deformed, $|\mathbb{Z}_3\rangle$ remains an eigenstate of $\mathcal{H}_f$ with the same energy. This may not necessarily still be the ground state and instead it may be shifted up in the energy spectrum for sufficiently large $\Delta V$. This means that upon quenching, the initial state remains the same over long periods due to its proximity to an eigenstate. As interaction distance is defined only with respect to a given state $\rho$, it is clear why it does not significantly change over time, despite quenching of the system across criticality. This interpretation is supported by the high overlap with a single eigenstate of the quench Hamiltonian in Fig. 4(a).

A similar argument can be made for why the quench from the $\mathbb{Z}_2$ initial state with $\mathcal{H}_f$ in the $\mathbb{Z}_3$ phase leads to scrambling and thermalization dynamics. As $\mathbb{Z}_2$ has an occupancy on every two lattice sites, it "feels" the deformation of $\Delta V$: $\mathcal{H}^{nn} |\mathbb{Z}_2\rangle = N/2 |\mathbb{Z}_2\rangle$. Considering the form of $\mathcal{H}_i$ such that the initial state is $|\mathbb{Z}_2\rangle$, the term that results in this being approximately the ground state is $\sum_{i=1}^{N} -|U|n_i - |V|n_i n_{i+2}$, with $U, V \gg \Omega$. For quenching with $\mathcal{H}_f$ in the $\mathbb{Z}_3$ regime, suitable tuning of positive $\Delta V$ then means that given $\mathcal{H}_f$, $|\mathbb{Z}_2\rangle$ is no longer an eigenstate due to the competing factors $U, V$ and $\Delta V$. More concretely, the final Hamiltonian when acting on $|\mathbb{Z}_2\rangle$ has a term proportional to $-(|U| + |V|) + \Delta V$. These competing negative and positive terms mean that, overall, $-(|U| + |V|) + \Delta V$ may not be much greater than $\Omega$ and $|\mathbb{Z}_2\rangle$ may no longer be approximately an eigenstate like before. This results in the possible scrambling of the initial state into a non-Gaussian state over time.

To further substantiate the previous argument, the underlying mechanism for persistent non-Gaussian correlations can be inferred by considering an effective quench Hamiltonian with five-body interactions. As we are interested in the quench dynamics going from $\mathbb{Z}_3$ into the $\mathbb{Z}_2$ ordered phase, we define the effective Hamiltonian in a

regime where $U$ is negative and large, favoring particle creation on all sites. Similarly, we require $V$ to be large and negative. Under these conditions, the quench Hamiltonian is given by

$$\mathcal{H}_q = - \left[ \sum_{i=1}^{N} \mathcal{P}_{i-1} \sigma_i^x \mathcal{P}_{i+1} + |U| n_i + |V| n_i, n_{i+2} \right] \quad (8)$$

with $|U| \gg 1$ and $|V| \gg 1$, and we still have $n_i n_{i+1} = 0$. Following a similar procedure as in Ref. [52], we move the quench Hamiltonian into an interaction picture with respect to the next-nearest-neighbor term by applying the transformation $W^\dagger \mathcal{H}_q W$, where $W = \exp[-it|V| \sum_i n_i n_{i+2}]$. Ignoring the rapidly oscillating phases for $|V| \gg 1$, we obtain an effective Hamiltonian

$$\mathcal{H}_q^{\text{eff}} = - \left[ \sum_{i=1}^{N} \mathcal{P}_{i-2} \mathcal{P}_{i-1} \sigma_i^x \mathcal{P}_{i+1} \mathcal{P}_{i+2} + |U| n_i \right]. \quad (9)$$

In the largest fully connected sector, the presence of Rydberg excitations on the nearest-neighboring and next-nearest-neighboring sites is prohibited. The effective Hamiltonian corresponds to the PPXPP model with a chemical potential. The $\mathbb{Z}_2$ state still exists as the overall ground state but instead exists within a small disconnected sector due to the new blockade condition. Meanwhile, because of a large negative $U$ in the effective Hamiltonian, the ground state of the largest sector where the blockade remains respected is $\mathbb{Z}_3$. Thus, the quench Hamiltonian does not induce delocalizing dynamics when the system is initialized in the $\mathbb{Z}_3$ state and such states are protected against both Gaussification and thermalization. We can therefore conclude that the persistent non-Gaussianity of the $\mathbb{Z}_3$ initial state equivalently arises from the effective blockade mechanism up to the next-nearest-neighbor excitations in the interaction picture. Agreement in dynamics was also tested and was found numerically between the exact Hamiltonian and the effective Hamiltonian. This further supports the notion that the initial state remains approximately an eigenstate of the quench Hamiltonian.

## VI. EXPERIMENTAL IMPLICATIONS

With the possible quantum information applications, it is important to test the robustness of the non-Gaussification with regard to external perturbations. This is particularly important because our results rely on the quantum superpositions of states with degenerate energies in the $\mathbb{Z}_3$ and $\mathbb{Z}_2$ phases. External perturbations may result in the superposition collapsing into an energetically favorable product state, thus removing any non-Gaussian correlations. Here we focus on three types of effect that are relevant for experimental implementations: (i) the stability against a single-site magnetic field or impurity $\varepsilon n_i$ with magnitude

$\varepsilon$; (ii) the effect of changing the chemical potential $U$ during the quench; (iii) the effect of long-range van der Waals interactions that are present in real systems but are ignored in Eq. (1).

Figure 5 shows the results obtained when we add the impurity term $\varepsilon n_i$ to the Hamiltonian in Eq. (1) on site $i = 4$. We choose this site along the chain as it is found to have the most substantial effect on the results, providing a qualitative lower bound for robustness. Despite the presence of an impurity, we see that qualitative features of the phase diagram remain preserved with impurity strength $\varepsilon = 10^{-4}$; see Fig. 5(a). This is a magnitude of error much larger than the detuning resolution of current quantum technology [53]. Furthermore, perturbations are generally characterized by their proportionality to the ground state gap. We find this order of magnitude to be comparable to the energy gap of the system (which decreases with $N$). This demonstrates that the non-Gaussian characteristics are protected nearly up to the same order as the energy gap in the system. It is natural that any larger magnitude of error would disrupt this as one would no longer be probing ground-state physics. Taking a single point in this
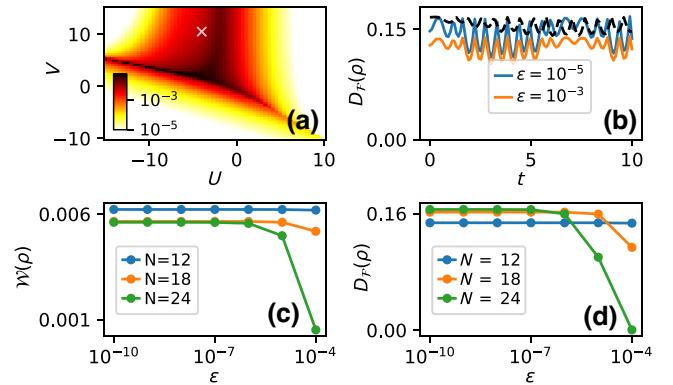


FIG. 5. Resilience of non-Gaussianity with regard to a local impurity, $\varepsilon n_4$, added to Eq. (1). (a) Phase diagram obtained with use of local Wick decomposition, $\mathcal{W}(\rho)$, with impurity strength $\varepsilon = 10^{-4}$ for system size $N = 12$. The cross marks the point $(U, V) = (-4, 10.5)$ studied in (b)–(d). (b) Time evolution of the interaction distance $D_\mathcal{F}$ for quenching of the initial ground state at $(U, V) = (-4, 10.5)$ in the $\mathbb{Z}_3$ phase with the Hamiltonian parameters $U = -4$ and $V = -6$ in the $\mathbb{Z}_2$ phase. Both the initial Hamiltonian and the quench Hamiltonian contain impurity $\varepsilon$. The data are for system size $N = 12$, with the impurity potentials shown in the legend. The dashed black line is with no error ($\varepsilon = 0$) but instead with the initial ground state taken at $(U, V) = (-15, 8)$ and quenching at $(U', V') = (-10, -5)$, which demonstrates persistent non-Gaussinity even with a change in $U$. (c),(d) Wick decomposition and interaction distance, respectively, of the ground state at $(U, V) = (-4, 10.5)$ as a function of impurity strength for several system sizes. The results were computed with exact diagonalization without resolving translation symmetry.

diagram, marked by the cross, we find the ground state still possesses high overlap with the superposition state $\mathbb{Z}_3$. Consequently, the non-Gaussian correlations persist for quenching in the $\mathbb{Z}_2$ phase (with error still present in the quench Hamiltonian), as seen in Fig. 5(b). For this point, the non-Gaussianity remains robust for impurity strengths $\varepsilon$ up to approximately $10^{-3}$. Furthermore, we test the robustness of $D_{\mathcal{F}}$ and $\mathcal{W}$ for this point with differing impurity strength and system size; see Figs. 5(c) and 5(d). The non-Gaussianity is seen to be more pronounced for smaller system sizes.

While our presented analysis assumes that only $V$ is changed during the quench, we have numerically verified that the non-Gaussian correlations also remain robust upon simultaneous changes in $U$. This can be understood via the following argument. Consider modulating both $V$ and $U$, then $\mathcal{H}_f |\mathbb{Z}_3\rangle = \mathcal{H}_i |\mathbb{Z}_3\rangle + \Delta U \mathcal{H}^n |\mathbb{Z}_3\rangle$, where $\mathcal{H}^n = \sum_i n_i$. Unlike $\mathcal{H}^{nn}$, $\mathcal{H}^n |\mathbb{Z}_3\rangle \neq 0$. This is instead equivalent to quenching horizontally in the phase diagram in Fig. 2; therefore, if $\Delta U$ is such that one remains in the regime where $|\mathbb{Z}_3\rangle$ is approximately the ground state, the state remains an eigenstate and the non-Gaussianity remains robust. This is illustrated by the dashed black line in Fig. 5, where in changing $V$ during the quench, we also take $\Delta U = 5$. On the other hand, if $\Delta U$ is large enough to transition from the $\mathbb{Z}_3$ regime, thermalization occurs. This stability regarding small changes in $U$ makes the non-Gaussianity effect robust with regard to possible experimental imperfections.

Finally, our idealized model in Eq. (1) ignores the long-range van der Waals forces that are invariably present in real systems of Rydberg atoms [27–29]. Thus, it is important to verify our conclusions still hold in the full model describing the Rydberg atom experiments [35]:

$$H = -\frac{\Omega}{2}\sum_i^N \sigma_i^x - U\sum_i^N n_i + V\sum_{i<j}\frac{n_i n_j}{|i-j|^6}. \quad (10)$$

Note that, in contrast to Eq. (1), here we keep the factor $1/2$ in the Rabi term and set $V = 1$ to facilitate comparison with the literature. We first recompute the Gaussianity phase diagram of the long-range model with relevant parameters taken from experimental papers [28,29]; see Fig. 6(a). Similarly to the truncated model in Eq. (1), the full model also realizes $\mathbb{Z}_3$ and $\mathbb{Z}_2$ phases. The phase diagram in Fig. 6(a) is in good agreement with that given in Ref. [35]. We then prepare the state in one phase (indicated by a red cross) and perform a quench into the other phase. As illustrated in Figs. 6(b) and 6(c), the results are consistent with those of the $U$-$V$ model, where the $\mathbb{Z}_3$ state preserves its non-Gaussian correlations. For the $\mathbb{Z}_2$ initial state, the thermalization timescale is longer than in Fig. 3 due to the smallness of the energy gap in the units
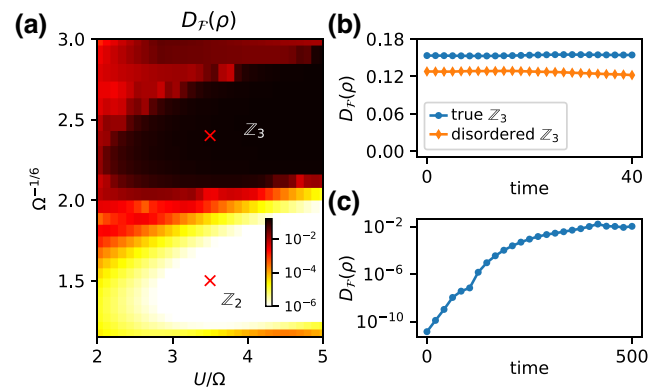


FIG. 6. (a) Gaussianity phase diagram of the long-range Rydberg model in Eq. (10) for system size $N = 12$ and fixed $V = 1$. (b),(c) Temporal behavior of $D_{\mathcal{F}}$ for quenching from the point indicated by the red cross in the $\mathbb{Z}_3$ ($\mathbb{Z}_2$) phase to the other phase. The different behavior of non-Gaussianity for the two types of quench, seen in Fig. 3, is reproduced. Blue lines indicate use of the pure Rydberg Hamiltonian (10). The orange line represents introduction of further experimental error by use of a Hamiltonian with spatial disorder such that $i,j \rightarrow i + \delta_i, j + \delta_j$, where $\delta$ is site dependent and taken randomly in the range $[-0.02, 0.02]$. The results are averaged over 100 realizations. Both the pure Rydberg Hamiltonian and the disordered Rydberg Hamiltonian show persistent non-Gaussinity.

chosen for the Hamiltonian (10). Taking this a step further, we introduce experimental error into our calculation. In Ref. [53] it is stated that there are errors of approximately 0.1 μm in the spatial position of sites along the Rydberg chain. We can factor this into our simulations by modulating $i,j \rightarrow i + \delta_i, j + \delta_j$ in Eq. (10) (so, numerically, $\delta$ is randomly sampled from a normal distribution between $-0.02$ and $0.02$). We find that the results still hold well when we take the initial ground state from a disordered Hamiltonian with only a slight decrease in $D_{\mathcal{F}}$ as shown by the orange line in Fig. 6(b). Moreover, if one assumes the perfect $\mathbb{Z}_3$ state can still be prepared, we find the perfect results still hold irrespective of the disordered quench Hamiltonian—adding a degree of robustness as it demonstrates the error only factors into the initial state preparation. Overall, the main features of our results are present in the full Rydberg model, suggesting that persistent non-Gaussianity could be observed with the existing experimental technology [28,29].

## VII. CONCLUSIONS

Quantum states can exhibit a Gaussian or non-Gaussian nature, depending on the degree of interaction between the system's constituent parts. In this work, we investigated the phenomenon of Gaussification, wherein non-Gaussian states undergo transformation into Gaussian states during quench dynamics in quantum many-body systems.

We showed that Rydberg atom arrays provide a versatile platform where this behavior can be probed with available experimental techniques. Perhaps more intriguingly, we demonstrated that the Rydberg blockade, intrinsic to such systems, gives rise to states with remarkably robust non-Gaussian correlations that persist far from equilibrium, for example, as the system is quenched across the quantum phase transition. We elucidated the origin of this behavior by analyzing quenches between the $\mathbb{Z}_2$ phase and the $\mathbb{Z}_3$ phase, which exhibit either scrambling dynamics or suppression of thermalization due to the effective Rydberg blockade mechanism. We formulated a criterion based on Wick decomposition that incorporates local correlations, providing a practical method for observing (non-)Gaussianity in experiments. This finding was further corroborated via variational optimization and computation of the minimal distance between the reduced density matrix of the ground states belonging to different ordered phases and the set of all free-fermion density matrices defined on the same subsystem.

Our results highlight the richness of quantum state complexity in systems evolving under constrained dynamics, and they provide three contributions to the broader quantum information framework. Firstly, our findings show the existence of robust non-Gaussian states in Rydberg systems, which are well-known resources for enhancing quantum information protocols. Recent studies have shown that non-Gaussian states act as magic states [14], facilitating the construction of a universal gate set. Our findings propose a route towards accessing and utilizing these robust states in the commonly explored Rydberg systems, moving closer to the realization of universal quantum devices, even in the presence of long-range interactions and local impurity potentials. Secondly, we demonstrate how Rydberg systems naturally generate and manipulate $\mathbb{Z}_3$ and $\mathbb{Z}_2$ states, which have a stark contrast in terms of their Gaussianity, due to the interplay between detuning and interactions. Particularly, we find that the $\mathbb{Z}_3$ state is maximally non-Gaussian while simultaneously robust regarding thermalization, which could serve as a qutrit basis for quantum memories [54,55]. Lastly, our results provide a constructive example that diverges from the typical Gaussification scenario in Refs. [18,23], thus illustrating the possibility of richer types of dynamical behavior facilitated by the Rydberg blockade.

In compliance with the EPSRC policy framework on research data, this publication is theoretical work that does not require supporting research data.

## APPENDIX A: MOTIVATION FOR THE CHOICE OF OPERATORS IN THE WICK DECOMPOSITION

We describe our motivation for the choice of $\hat{A}$, $\hat{B}$, $\hat{C}$, and $\hat{D}$ in Eq. (4), which yielded results qualitatively similar to the interaction distance across the three phases of the diagram. These operators must be single-site fermionic operators to provide a valid four-point Wick decomposition. To express these operators in terms of Pauli matrices, we use the Jordan-Wigner transformation. This allows us to reinterpret the fermionic creation and annihilation operators at site $j$ as spin-raising and spin-lowering operators, multiplied by the string $\prod_{k<j} \sigma_k^z$. This ensures the fermionic commutation relationship still holds.

We conducted an exhaustive search to verify the Wick decomposition in the $U$-$V$ model in Eq. (1), specifically where the Wick value in the $\mathbb{Z}_3$ state exceeds the Wick value in the $\mathbb{Z}_2$ state. Interestingly, no two-point Pauli correlations that can indicate Gaussianity in the model were found. This unique feature arises from the Rydberg blockade mechanism, setting it apart from other models, such as the $\mathbb{Z}_2$ phases in the transverse field Ising model.

However, several Wick decompositions involving three-point local Pauli decompositions successfully quantify Gaussianity. We discuss a specific choice here: $\hat{A} = f_1^\dagger$, $\hat{B} = f_1$, $\hat{C} = f_2^\dagger$, and $\hat{D} = f_3$. The left-hand side of Eq. (4), $\langle n_1 \sigma_2^+ \sigma_3^- \rangle$, invariably vanishes for the model due to the Rydberg blockade in the case of $\mathbb{Z}_2$ and due to the action of $\sigma_3^-$ on the spin-down state in the $\mathbb{Z}_3$ regime. Thus, the difference in Gaussianity originates from the right-hand side. To further exemplify and understand this, consider $N = 3$ and take both the Greenberger-Horne-Zeilinger (GHZ) state, $|\text{GHZ}\rangle = (|000\rangle + |111\rangle)/\sqrt{2}$ (which is a macroscopic superposition like $|\mathbb{Z}_2\rangle$), and the W state, $|\text{W}\rangle = (|100\rangle + |010\rangle + |001\rangle)/\sqrt{3}$ (similar to $|\mathbb{Z}_3\rangle$). For both states, because of the definition of the spin ladder operators and the form of the superpositions, $\langle n_1 \sigma_2^+ \sigma_3^- \rangle$ and $\langle \sigma_1^+ \sigma_2^+ \rangle \langle \sigma_1^- \sigma_2^z \sigma_3^- \rangle$ are zero. This leaves the $\langle n_1 \rangle \langle \sigma_2^+ \sigma_3^- \rangle$ and $\langle \sigma_1^- \sigma_2^+ \rangle \langle \sigma_1^+ \sigma_2^z \sigma_3^- \rangle$ components, which consist of simple particle-hopping terms (with no $n_1$ constraint unlike in $\langle n_1 \sigma_2^+ \sigma_3^- \rangle$). Both these terms are still found to be zero in the case of the GHZ state but nonzero in the case of the W state because we can change from one translated pair to another by simply flipping two spins—something that is not possible in the GHZ state due to the macroscopic superposition. This natural distinction between the GHZ state and the W state due to simple particle hopping is the motivation for this choice of $\hat{A}$, $\hat{B}$, $\hat{C}$, and $\hat{D}$ for these states.

Recomputing the diagram using purely these two distinguishing hopping terms yields a result that qualitatively matches the interaction distance diagram in Fig. 2.

## APPENDIX B: OPEN BOUNDARY CONDITIONS AND FINITE-SIZE SCALING

We also examined the Gaussianity phase diagram for OBCs and the scaling of the non-Gaussian correlations with system size. Notably, under OBCs, the system no longer retains translational invariance and momentum is no longer a good quantum number. The translation invariance is broken by the boundary terms, which we take to be $\sigma_1^x P_2$ and $P_{N-1}\sigma_N^x$. The dimension of the Hilbert space is also larger than that under PBCs, since states such as $|10101\rangle$ are permissible under OBCs, while the Rydberg blockade precludes these under PBCs. Moreover, in the OBC context, spontaneous symmetry breaking leads to the absence of exact ground state degeneracy, resulting in the system selecting a nondegenerate ground state.

We find that to obtain sensible results from our local Wick decomposition in the OBC case, we need to use odd system sizes to properly capture the $\mathbb{Z}_2$ ground state of the form $|1010\cdots101\rangle$ and with $N$ divisible by 3 to allow for the $\mathbb{Z}_3$ phase. This ensures that excitations will be localized at the edges and the bulk behavior will accurately reflect the underlying physics. Wick decomposition, implemented with use of Eq. (5), can conveniently probe this. Here, because of OBCs, we evaluate local correlations only within the bulk of the system so as to avoid the boundary effects where the Rydberg blockade is slightly weaker. The Gaussianity phase diagrams, depicted in Fig. 7, demonstrate excellent agreement with the PBC results in terms of both interaction distance and local Wick decomposition in Eq. (5).

Finally, we investigated the interaction distance for larger system sizes undergoing quench dynamics from the $\mathbb{Z}_3$ phase to the $\mathbb{Z}_2$ phase. As can be seen in Fig. 8, the



FIG. 8. Temporal behavior of interaction distance under quench dynamics from the $\mathbb{Z}_3$ state ($V_i = 8$) to the $\mathbb{Z}_2$ phase ($V_f = -5$) with fixed $U = -15$. The data are for system sizes $N = 18$, $N = 24$, and $N = 30$. The inset shows the scaling of minimum $D_{\mathcal{F}}$ as a function of system size.

non-Gaussianity becomes more pronounced with increasing system size at moderate times $t \lesssim 15$. As the system size increases, the oscillation amplitudes are observed to decrease. Thus, for large system sizes, we anticipate an essentially constant $D_{\mathcal{F}}$ value with small fluctuations around it.
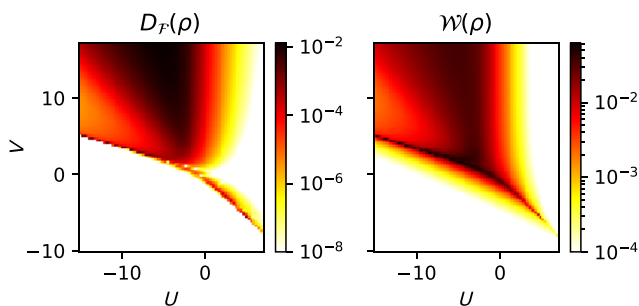


FIG. 7. Gaussianity phase diagrams for OBCs. They are analogous to Figs. 2(a) and 2(b) with interaction distance and Wick decomposition computed according to Eqs. (6) and (5), respectively. The system size $N = 15$ and the Wick decomposition is computed for operators on sites 7, 8, and 9 in the bulk of the chain.
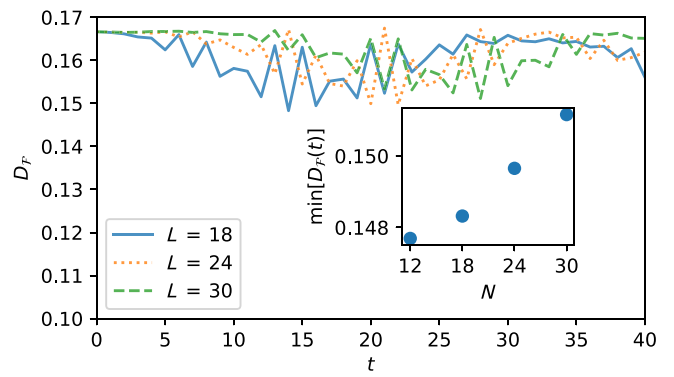
[1] G. C. Wick, The evaluation of the collision matrix, Phys. Rev. **80**, 268 (1950).

[2] M. E. Peskin and D. V. Schroeder, *An Introduction to Quantum Field Theory* (Addison-Wesley, Reading, USA, 1995).

[3] D. E. Browne, J. Eisert, S. Scheel, and M. B. Plenio, Driving non-Gaussian to Gaussian states with linear optics, Phys. Rev. A **67**, 062320 (2003).

[4] S. L. Braunstein and P. van Loock, Quantum information with continuous variables, Rev. Mod. Phys. **77**, 513 (2005).

[5] N. C. Menicucci, P. van Loock, M. Gu, C. Weedbrook, T. C. Ralph, and M. A. Nielsen, Universal quantum computation with continuous-variable cluster states, Phys. Rev. Lett. **97**, 110501 (2006).

[6] J. Heersink, C. Marquardt, R. Dong, R. Filip, S. Lorenz, G. Leuchs, and U. L. Andersen, Distillation of squeezing from non-Gaussian quantum states, Phys. Rev. Lett. **96**, 253601 (2006).

[7] J. Niset, J. Fiurášek, and N. J. Cerf, No-go theorem for Gaussian quantum error correction, Phys. Rev. Lett. **102**, 120501 (2009).

[8] R. M. Gomes, A. Salles, F. Toscano, P. H. Souto Ribeiro, and S. P. Walborn, Quantum entanglement beyond Gaussian criteria, Proc. Natl. Acad. Sci. **106**, 21517 (2009).

[9] A. Mari and J. Eisert, Positive Wigner functions render classical simulation of quantum computation efficient, Phys. Rev. Lett. **109**, 230503 (2012).

[10] M. Walschaers, C. Fabre, V. Parigi, and N. Treps, Entanglement and Wigner function negativity of multimode non-Gaussian states, Phys. Rev. Lett. **119**, 183601 (2017).

[11] D. Su, C. R. Myers, and K. K. Sabapathy, Conversion of Gaussian states to non-Gaussian states using photon-number-resolving detectors, Phys. Rev. A **100**, 052301 (2019).

[12] Y.-S. Ra, A. Dufour, M. Walschaers, C. Jacquard, T. Michel, C. Fabre, and N. Treps, Non-Gaussian quantum states of a multimode light field, Nat. Phys. **16**, 144 (2020).

[13] M. Walschaers, Non-Gaussian quantum states and where to find them, PRX Quantum **2**, 030204 (2021).

[14] M. Hebenstreit, R. Jozsa, B. Kraus, S. Strelchuk, and M. Yoganathan, All pure fermionic non-Gaussian states are magic states for matchgate computations, Phys. Rev. Lett. **123**, 080503 (2019).

[15] J. K. Verma, L. Lachman, and R. Filip, Direct detection of quantum non-Gaussian light from a dispersively coupled single atom, Quantum **6**, 660 (2022).

[16] M. Gluza, C. Krumnow, M. Friesdorf, C. Gogolin, and J. Eisert, Equilibration via Gaussification in fermionic lattice systems, Phys. Rev. Lett. **117**, 190602 (2016).

[17] F. Carollo, Non-Gaussian dynamics of quantum fluctuations and mean-field limit in open quantum central spin systems, arXiv:2305.15547 [cond-mat.stat-mech] (2023).

[18] M. Cramer, C. M. Dawson, J. Eisert, and T. J. Osborne, Exact relaxation in a class of nonequilibrium quantum lattice systems, Phys. Rev. Lett. **100**, 030602 (2008).

[19] M. Cramer and J. Eisert, A quantum central limit theorem for non-equilibrium systems: exact local relaxation of correlated states, New J. Phys. **12**, 055020 (2010).

[20] M. Gluza, T. Schweigler, M. Tajik, J. Sabino, F. Cataldini, F. S. Møller, S.-C. Ji, B. Rauer, J. Schmiedmayer, J. Eisert, and S. Sotiriadis, Mechanisms for the emergence of Gaussian correlations, SciPost Phys. **12**, 113 (2022).

[21] T. Schweigler, V. Kasper, S. Erne, I. Mazets, B. Rauer, F. Cataldini, T. Langen, T. Gasenzer, J. Berges, and J. Schmiedmayer, Experimental characterization of a quantum many-body system via higher-order correlations, Nature **545**, 323 (2017).

[22] T. Schweigler, M. Gluza, M. Tajik, S. Sotiriadis, F. Cataldini, S.-C. Ji, F. S. Møller, J. Sabino, B. Rauer, J. Eisert, and J. Schmiedmayer, Decay and recurrence of non-Gaussian correlations in a quantum many-body system, Nat. Phys. **17**, 559 (2021).

[23] C. Gogolin and J. Eisert, Equilibration, thermalisation, and the emergence of statistical mechanics in closed quantum systems, Rep. Prog. Phys. **79**, 056001 (2016).

[24] A. Polkovnikov, K. Sengupta, A. Silva, and M. Vengalattore, Colloquium: Nonequilibrium dynamics of closed interacting quantum systems, Rev. Mod. Phys. **83**, 863 (2011).

[25] A. Browaeys and T. Lahaye, Many-body physics with individually controlled Rydberg atoms, Nat. Phys. **16**, 132 (2020).

[26] H. Labuhn, D. Barredo, S. Ravets, S. de Léséleuc, T. Macrì, T. Lahaye, and A. Browaeys, Tunable two-dimensional arrays of single Rydberg atoms for realizing quantum Ising models, Nature **534**, 667 (2016).

[27] H. Bernien, S. Schwartz, A. Keesling, H. Levine, A. Omran, H. Pichler, S. Choi, A. S. Zibrov, M. Endres, M. Greiner, V. Vuletic, and M. D. Lukin, Probing many-body dynamics on a 51-atom quantum simulator, Nature **551**, 579 (2017).

[28] A. Keesling, A. Omran, H. Levine, H. Bernien, H. Pichler, S. Choi, R. Samajdar, S. Schwartz, P. Silvi, S. Sachdev, P. Zoller, M. Endres, M. Greiner, V. Vuletić, and M. D. Lukin, Quantum Kibble–Zurek mechanism and critical dynamics on a programmable Rydberg simulator, Nature **568**, 207 (2019).

[29] A. Omran, H. Levine, A. Keesling, G. Semeghini, T. T. Wang, S. Ebadi, H. Bernien, A. S. Zibrov, H. Pichler, S. Choi, J. Cui, M. Rossignolo, P. Rembold, S. Montangero, T. Calarco, M. Endres, M. Greiner, V. Vuletić, and M. D. Lukin, Generation and manipulation of Schrödinger cat states in Rydberg atom arrays, Science **365**, 570 (2019).

[30] C. J. Turner, K. Meichanetzidis, Z. Papić, and J. K. Pachos, Optimal free descriptions of many-body theories, Nat. Commun. **8**, 14926 (2017).

[31] P. Fendley, K. Sengupta, and S. Sachdev, Competing density-wave orders in a one-dimensional hard-boson model, Phys. Rev. B **69**, 075106 (2004).

[32] I. Lesanovsky and H. Katsura, Interacting Fibonacci anyons in a Rydberg gas, Phys. Rev. A **86**, 041601(R) (2012).

[33] C. J. Turner, A. A. Michailidis, D. A. Abanin, M. Serbyn, and Z. Papic, Weak ergodicity breaking from quantum many-body scars, Nat. Phys. **14**, 745 (2018).

[34] R. Samajdar, S. Choi, H. Pichler, M. D. Lukin, and S. Sachdev, Numerical study of the chiral $F_3$ quantum phase transition in one spatial dimension, Phys. Rev. A **98**, 023614 (2018).

[35] M. Rader and A. M. Lauchli, Floating phases in one-dimensional Rydberg Ising chains, arXiv e-print arXiv:1908.02068 (2019).

[36] N. Chepiga and F. Mila, Floating phase versus chiral transition in a 1D hard-boson model, Phys. Rev. Lett. **122**, 017205 (2019).

[37] R. J. Baxter, Hard hexagons: Exact solution, J. Phys. A: Math. Gen. **13**, L61 (1980).

[38] K. Slagle, D. Aasen, H. Pichler, R. S. K. Mong, P. Fendley, X. Chen, M. Endres, and J. Alicea, Microscopic characterization of Ising conformal field theory in Rydberg chains, Phys. Rev. B **104**, 235109 (2021).

[39] J. K. Pachos and Z. Papic, Quantifying the effect of interactions in quantum many-body systems, SciPost Phys. Lect. Notes, 4 (2018).

[40] G. Matos, A. Hallam, A. Deger, Z. Papić, and J. K. Pachos, Emergence of gaussianity in the thermodynamic limit of interacting fermions, Phys. Rev. B **104**, L180408 (2021).

[41] J. K. Pachos and C. Vlachou, Quantifying fermionic interactions from the violation of Wick's theorem, Quantum **6**, 840 (2022).

[42] H. Li and F. D. M. Haldane, Entanglement spectrum as a generalization of entanglement entropy: Identification of topological order in non-Abelian fractional quantum Hall effect states, Phys. Rev. Lett. **101**, 010504 (2008).

[43] I. Peschel, Calculation of reduced density matrices from correlation functions, J. Phys. A: Math. Gen. **36**, L205 (2003).

[44] K. Meichanetzidis, C. J. Turner, A. Farjami, Z. Papić, and J. K. Pachos, Free-fermion descriptions of parafermion chains and string-net models, Phys. Rev. B **97**, 125104 (2018).

[45] M. Ueda, Quantum equilibration, thermalization and prethermalization in ultracold atoms, Nat. Rev. Phys. **2**, 669 (2020).

[46] M. Serbyn, D. A. Abanin, and Z. Papić, Quantum many-body scars and weak breaking of ergodicity, Nat. Phys. **17**, 675 (2021).

[47] S. Moudgalya, B. A. Bernevig, and N. Regnault, Quantum many-body scars and Hilbert space fragmentation: a review of exact results, Rep. Prog. Phys. **85**, 086501 (2022).

[48] A. Chandran, T. Iadecola, V. Khemani, and R. Moessner, Quantum many-body scars: A quasiparticle perspective, Annu. Rev. Condens. Matter Phys. **14**, 443 (2023).

[49] I. Bloch, J. Dalibard, and W. Zwerger, Many-body physics with ultracold gases, Rev. Mod. Phys. **80**, 885 (2008).

[50] M. Kormos, M. Collura, G. Takács, and P. Calabrese, Real-time confinement following a quantum quench to a non-integrable model, Nat. Phys. **13**, 246 (2017).

[51] I.-C. Chen and T. Iadecola, Emergent symmetries and slow quantum dynamics in a Rydberg-atom chain with confinement, Phys. Rev. B **103**, 214304 (2021).

[52] I. Lesanovsky, Many-body spin interactions and the ground state of a dense Rydberg lattice gas, Phys. Rev. Lett. **106**, 025301 (2011).

[53] J. Wurtz, A. Bylinskii, B. Braverman, J. Amato-Grill, S. H. Cantu, F. Huber, A. Lukin, F. Liu, P. Weinberg, J. Long, S.-T. Wang, N. Gemelke, and A. Keesling, Aquila: QuEra's 256-qubit neutral-atom quantum computer, arXiv:2306.11727 [quant-ph] (2023).

[54] B. J. Brown, D. Loss, J. K. Pachos, C. N. Self, and J. R. Wootton, Quantum memories at finite temperature, Rev. Mod. Phys. **88**, 045005 (2016).

[55] S. Goel, M. Reynolds, M. Girling, W. McCutcheon, S. Lee-dumrongwatthanakun, V. Srivastav, D. Jennings, M. Malik, and J. K. Pachos, Unveiling the non-Abelian statistics of $d(s_3)$ anyons via photonic simulation, arXiv:2304.05286 [quant-ph] (2023).